

## An Educational Platform for Small Satellite Development with Proximity Operation Capabilities

Ivan R. Bertaska and John Rakoczy  
 NASA Marshall Space Flight Center  
 Mailstop EV41 Huntsville, AL 35812; (256) 544-6427  
 ivan.r.bertaska@nasa.gov

### ABSTRACT

An alternative to ground testing of small satellites is presented here, where the kinematics of a 3U underactuated CubeSat operating in 3 degrees-of-freedom (DOF) is reproduced by an omnidirectional wheeled platform, while satellite dynamics are simulated in real-time. The system is equipped with a relative navigation sensor in the form factor of a smartphone, the Smartphone Video Guidance Sensor (SVGS), allowing the platform to reproduce proximity operation maneuvers. The wheeled platform is used as an educational tool for students over a large range of academic levels, from high school to graduate school. A derivation of the kinematic relationship from satellite dynamics to rotacaster wheel velocities is presented, along with the guidance and control laws of the system. Simulation and experimental results demonstrate that the wheeled platform was able to successfully replicate detumble, slew, and attitude hold maneuvers of a 3U CubeSat.

### INTRODUCTION

Long term goals for small satellites seek to utilize their force multiplier potential, where systems of small satellites provide a cost-effective alternative to monolithic systems. To achieve these goals, small satellites will need to work in close proximity under careful coordination. Traditional means to validate the mission planning and GNC of these small satellite networks use a combination of simulations and three degree-of-freedom (3DOF) experiments on air bearings floating over sufficiently flat surfaces. This method closes the loop around the system dynamics, but brings additional complexity, as the full system, along with all sensors and flight software, needs to be tested. The size of the flat surface will define the mission area and restrict the capabilities that can be validated. The capacity of pressurized tanks and length of air supply hoses may further limit capabilities.

An alternative solution is presented here, where satellite kinematics are simulated on a 3DOF, wheeled platform, allowing for the rapid prototyping and development of proximity operation logic. Closing the loop around the system kinematics removes the overhead in testing the full system – only the mission planning, GNC, and ADCS/navigation sensors are integrated. A key benefit is that GNC and proximity operation logic can be rapidly reiterated and deployed on the platform, allowing for debugging support and a partial physical realization. This combined system is referred to as the Agilis Small Satellite Kinematic Simulator (ASKS) in this text.

The wheeled vehicle simulator uses a Lego Mindstorm/EV3 construction with rotacaster wheels (“Agilis”), allowing for a full 3DOF range of motion. A navigation stack common to small satellites can be mounted on the Agilis, complete with a Xiphos Q7 board running the GNC system. A relative navigation sensor is installed in each unit capable of providing the relative orientation and position. The chosen relative navigation sensor is the Smartphone Video Guidance Sensor (SVGS) – a proximity operation sensor in a smartphone form factor<sup>1</sup>. The SVGS uses a known target pattern modeled by either retroreflectors or LEDs, to produce the relative orientation and position between a camera and the target. It can be utilized as a proximity operations or autonomous rendezvous visual sensor. The target

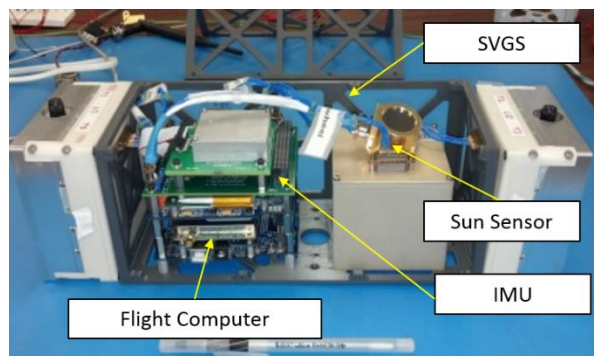


**Figure 1 – The air-bearing enabled, floating 3U CubeSat platform. GNC sensors include an IMU, a sun sensor, and an SVGS (not pictured). This platform and its navigation stack is emulated on the Agilis LEGO-based platform.**

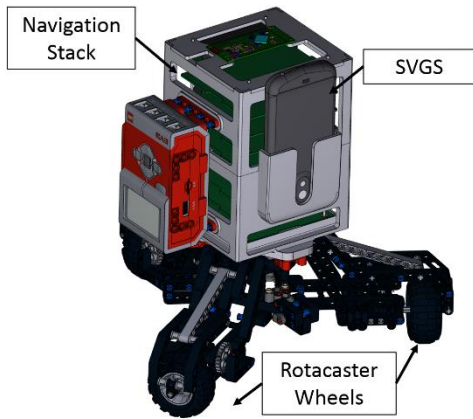


**Figure 2 – The Agilis platform with a SVGS sensor and a navigation stack. Included on the navigation stack are the flight computer, battery and EPS, and IMU.**

pattern is mounted on the “target” spacecraft, while the “chaser” spacecraft houses the camera and associated avionics (in this case, a smartphone). The “chaser” spacecraft can then rendezvous with the “target” using feedback from the SVGS in conjunction with traditional proximity operations sensors, like LIDARs.

In this work, an ASKS platform is designed to simulate a “3U” (30cm x 10cm x 10cm) satellite floating on air bearings performing proximity operations. The ASKS is outfitted with a similar sensor suite as a traditional CubeSat (relative navigation sensor, gyroscope, and accelerometer). Satellite dynamics are simulated onboard the ASKS, and spacecraft body velocities and rotation rates are converted to ASKS wheel velocities. Thus, only the kinematics of the system are tested in closed-loop. Both simulation results of the 3U CubeSat and experimental results with the ASKS are presented here. Figure 1 displays the 3U CubeSat bus with key components annotated. Two 0.5U propulsion units bookend the inner avionics housing. Thrusters are oriented such that a forces can be applied in the lateral direction, but not in the longitudinal direction. Thus, the 3U system is considered to be underactuated. Figure 2 shows the Agilis platform equipped with both the 3U navigation stack and the SVGS proximity operations sensor. Not pictured is an SVGS target pattern with retroreflectors on the rear of the vehicle.

This project doubles as an educational platform where students at all levels, from primary school to university, have an opportunity to contribute to development and create a knowledgebase around small satellites. Using the combination of LEGO products and a smartphone based visual navigation sensor provides students with familiar concepts as a launching point for further

progress. Tying these systems with Robot Operating System (ROS) creates an environment with a graphical front end and an active online community, permitting access to ample resources for novice users. This text details the development of the ASKS and educational impact of this approach.

The paper is structured as follows: the first section presents the equations of motion of the 3DOF planar satellite, as well as the derivation of the kinematics of the omnidirectional Agilis platform. Additionally, guidance and control laws are detailed here. The second section describes SVGS and its underlying mathematics. The 3U CubeSat avionics architecture is described in the third section, and its software architecture in the fourth section. The fifth section presents simulation and experimental results, and the sixth section gives an overview of the educational impact of this project. The last section concludes this work with some closing remarks and descriptions of the future direction of this project.

## DYNAMICS, KINEMATICS, AND GNC

### *Satellite Rigid Body Dynamics*

The dynamics of the simulated satellite can be expressed through the traditional rigid body equations of motion. More complex dynamics, such as flexible body and sloshing, can be included as dictated by the mission. The presentation of the spacecraft dynamics follows the same notation as Terui<sup>2</sup>, with  $r_I = [x_I, y_I, z_I]^T \in \mathbb{R}^3$  representing the position of the chaser spacecraft relative to an inertial frame,  $v = [u, v, w]^T \in \mathbb{R}^3$  representing the body velocities,  $\omega = [\omega_x, \omega_y, \omega_z]^T \in \mathbb{R}^3$  representing the body rates, and  $\theta' = [\phi, \theta, \psi]^T \in \mathbb{S}^3$  representing the 3-2-1 Euler angles of the spacecraft. Figure 3 displays the body frame of the spacecraft,  $\{x_b, y_b\}$ , and the inertial frame,  $\{x, y\}$ . The quaternion representation of the vehicle attitude is neglected in this presentation, as the ASKS platform is constrained to operate on 3DOF planar motion and will not suffer from a singularity.

For proximity operations under a sufficiently small separation between spacecraft, orbital dynamics may be neglected. A reference frame moving with both spacecraft, such as the Clohessy-Wiltshire frame<sup>3</sup>, is typically chosen. Since the ASKS platform mimics the kinematics of a flat-floor satellite test, all equations of motion are derived assuming an inertially fixed coordinate system coincident with the target frame. The rigid body dynamics can be expressed as,

$$m'\dot{v} + m'\omega \times v = f, \quad (1)$$

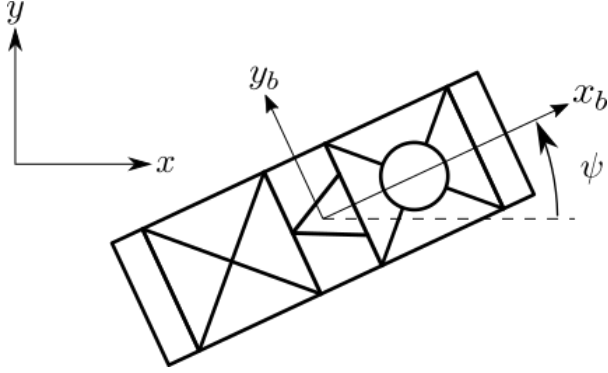


**Figure 3 – The 3DOF planar motion CubeSat body coordinate system ( $\{x_b, y_b\}$ ) and inertial coordinate system ( $\{x, y\}$ ). Controlled vehicle states are yaw  $\psi$  and yaw rate  $\omega_z$ , inertial position  $x$  and  $y$ , and body velocities  $u$  and  $v$ .**

$$I\dot{\omega} + \omega^\times I\omega = \rho^\times f + \tau, \quad (2)$$

where the  $\times$  superscript is the matrix representation of the cross product of the annotated vector. Thus,  $\omega^\times \in \mathbb{R}^{3 \times 3}$  is,

$$\omega^\times = \begin{bmatrix} 0 & -\omega_z & \omega_y \\ \omega_z & 0 & -\omega_x \\ -\omega_y & -\omega_x & 0 \end{bmatrix}. \quad (3)$$

$I \in \mathbb{R}^{3 \times 3}$  is the inertial matrix,  $m' \in \mathbb{R}^{3 \times 3}$  is the diagonal mass matrix,  $f = [f_x, f_y, f_z] \in \mathbb{R}^3$  is the vector of control and disturbance forces, and  $\tau = [\tau_x, \tau_y, \tau_z] \in \mathbb{R}^3$  is the vector of other torques on the vehicle (e.g., reaction wheel torques, disturbance torques, etc.). The 3-2-1 Euler angle rates and inertial velocities are obtained from the following,

$$\dot{\theta}' = \begin{bmatrix} \dot{\phi} \\ \dot{\theta} \\ \dot{\psi} \end{bmatrix} = \begin{bmatrix} 1 & \sin\phi \tan\theta & \cos\phi \tan\theta \\ 0 & \cos\phi & -\sin\phi \\ 0 & \sin\phi \sec\theta & \cos\phi \sec\theta \end{bmatrix} \begin{bmatrix} \omega_x \\ \omega_y \\ \omega_z \end{bmatrix}, \quad (4)$$

$$\dot{r}_i = T_B^I v, \quad (5)$$

$$T_B^I = \begin{bmatrix} c\theta c\psi & -c\phi s\psi + s\phi s\theta c\psi & s\phi s\psi + c\phi s\theta c\psi \\ c\theta s\psi & c\phi c\psi + s\phi s\theta s\psi & -s\phi c\psi + c\phi s\theta s\psi \\ -s\theta & s\phi c\theta & c\phi c\theta \end{bmatrix}.$$

Where  $\cos$  and  $\sin$  have been abbreviated as  $c$  and  $s$ , respectively. The planar motion of the platform restricts the spacecraft in the  $z_b$  axis, which leads to constraints on  $\omega_x$ ,  $\omega_y$ , and  $w$ . The reduced nonlinear rigid body dynamics can then be expressed in a state equation,

$$\begin{bmatrix} m & 0 & 0 \\ 0 & m & 0 \\ 0 & 0 & I_{zz} \end{bmatrix} \begin{bmatrix} \dot{u} \\ \dot{v} \\ \dot{\omega}_z \end{bmatrix} = \begin{bmatrix} 0 & 0 & -mv \\ 0 & 0 & mu \\ mv & -mu & 0 \end{bmatrix} \begin{bmatrix} u \\ v \\ r \end{bmatrix} + \begin{bmatrix} f_x \\ f_y \\ \tau_z \end{bmatrix}, \quad (6)$$

$$\begin{bmatrix} \dot{x}_i \\ \dot{y}_i \\ \dot{\psi} \end{bmatrix} = \begin{bmatrix} \cos\psi & -\sin\psi & 0 \\ \sin\psi & \cos\psi & 0 \\ 0 & 0 & 1 \end{bmatrix} \begin{bmatrix} u \\ v \\ \omega_z \end{bmatrix}. \quad (7)$$

### Omnidirectional Wheeled Robot Kinematics

The derivation of the multi-wheeled vehicle kinematics equations roughly follows that of Garcia-Sillas, et al.<sup>4</sup>. A wheel frame is chosen as shown in Figure 4, with the  $y_i$ -axis collinear with the axis of rotation of the main hub and  $x_i$ -axis in the direction of travel. Let  $R \in \mathbb{R}^+$  be the radius of the main hub,  $r \in \mathbb{R}^+$  be the radius of the roller on the rotacaster wheel, and  $L \in \mathbb{R}^+$  be the length of the arm from the center of the Agilis platform to the point of contact of each wheel (see Figure 5). Knowing that the rotational axis of the roller is orthogonal to that of the main hub, a transformation from the wheel angular velocity  $\omega_{iy} \in \mathbb{R} \forall i \in \{1,2,3\}$ , roller angular velocity  $\omega_{ir} \in \mathbb{R}$ , and the planar rotation rate of the wheel,  $\omega_{iz}$  into the wheel velocities and rotation rates is defined as,

$$\begin{bmatrix} V_{ix} \\ V_{iy} \\ \omega_{iz} \end{bmatrix} = \begin{bmatrix} R & 0 & 0 \\ 0 & r & 0 \\ 0 & 0 & 1 \end{bmatrix} \begin{bmatrix} \omega_{iy} \\ \omega_{ir} \\ \omega_{iz} \end{bmatrix}. \quad (8)$$

The rotation rates of the wheel and roller, and the corresponding velocities and rotation rates at the wheel can be defined as  $\hat{q}_i = [\omega_{iy}, \omega_{ir}, \omega_{iz}]^T \in \mathbb{R}^3$  and  $\hat{q}_i = [V_{ix}, V_{iy}, \omega_{iz}]^T \in \mathbb{R}^3$  respectively.

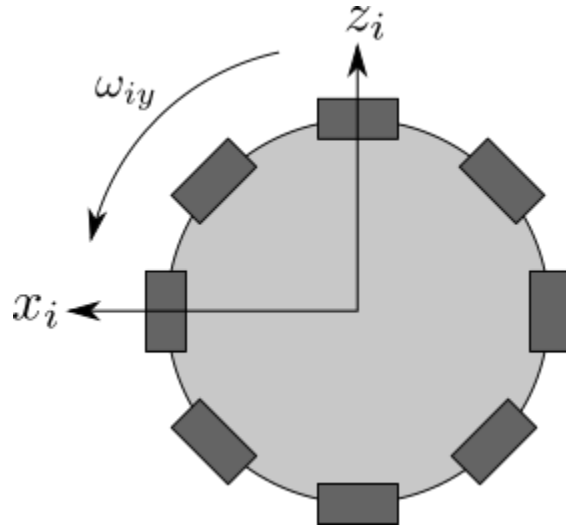


**Figure 4 – Wheel coordinate frame with positive wheel angular velocity  $\omega_{iy}$  denoted.**

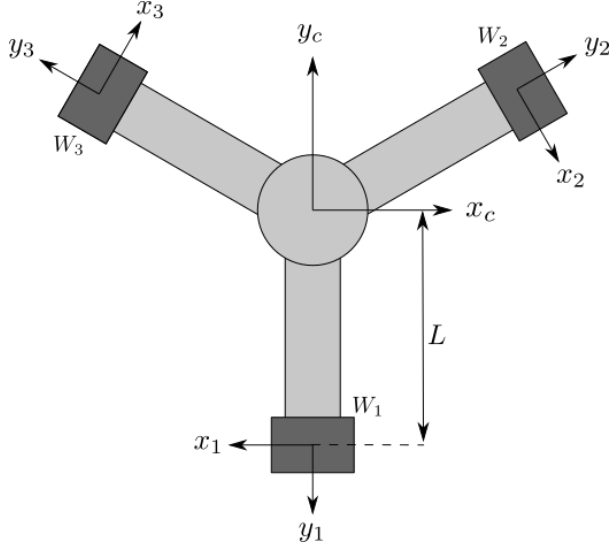


**Figure 5 – The Agilis platform frame. The  $\{x_c, y_c\}$  frame is located at the geometric center of the vehicle and assumed to be the instantaneous center of rotation.  $\{x_i, y_i\} \forall i \in \{1, 2, 3\}$  is the coordinate system for each wheel whose  $y_i$ -axis is collinear with the axis of rotation.**

Examining Figure 5, the kinematic relationship between any individual wheel,  $W_i$ , and the geometric center of the Agilis  $c$  is given as,

$$\begin{bmatrix} V_{ix} \\ V_{iy} \\ \omega_{iz} \end{bmatrix} = \begin{bmatrix} \cos\alpha & -\sin\alpha & p_y \\ \sin\alpha & \cos\alpha & -p_x \\ 0 & 0 & 1 \end{bmatrix} \begin{bmatrix} \omega_{iy} \\ \omega_{ir} \\ \omega_{iz} \end{bmatrix}. \quad (9)$$

where  $V_{ix} \in \mathbb{R}$ ,  $V_{iy} \in \mathbb{R}$ , and  $\omega_{iz} \in \mathbb{R}$  are the x linear velocity, the y linear velocity, and the planar rotation in the wheel frame, respectively.  $p_x \in \mathbb{R}$  and  $p_y \in \mathbb{R}$  are the x and y coordinates of each wheel hub  $W_i$ .  $\alpha \in \mathbb{S}$  is the rotation from the body frame to the wheel frame. Combining (8) and (9) yields,

$$\begin{bmatrix} u_c \\ v_c \\ \omega_{cz} \end{bmatrix} = \begin{bmatrix} R \cos\alpha_i & -r \sin\alpha_i & p_{iy} \\ R \sin\alpha_i & r \cos\alpha_i & -p_{ix} \\ 0 & 0 & 1 \end{bmatrix} \begin{bmatrix} \omega_{iy} \\ \omega_{ir} \\ \omega_{iz} \end{bmatrix}, \quad (10)$$

$$\Rightarrow \hat{q}_i = J_i \dot{q}_i, \quad (11)$$

where  $J_i \in \mathbb{R}^{3 \times 3}$  represents the transformation in (10). A relation is built from each wheel state velocity vector  $\dot{q} = [\dot{q}_1, \dot{q}_2, \dot{q}_3]^T \in \mathbb{R}^9$  to the body velocities  $\dot{q}_c = [u_c, v_c, \omega_{cz}]^T \in \mathbb{R}^3$ ,

$$\begin{bmatrix} I_{3 \times 3} \\ I_{3 \times 3} \\ I_{3 \times 3} \end{bmatrix} \begin{bmatrix} u_c \\ v_c \\ \omega_{cz} \end{bmatrix} = \begin{bmatrix} J_1 & 0_{3 \times 3} & 0_{3 \times 3} \\ 0_{3 \times 3} & J_2 & 0_{3 \times 3} \\ 0_{3 \times 3} & 0_{3 \times 3} & J_3 \end{bmatrix} \begin{bmatrix} \dot{q}_1 \\ \dot{q}_2 \\ \dot{q}_3 \end{bmatrix}, \quad (12)$$

$$\Rightarrow A \dot{q}_c = B \dot{q} \quad (13)$$

where  $0_{3 \times 3}$  and  $I_{3 \times 3}$  are the null and identity matrices. The goal is to find the kinematic relationship between the velocities of the body  $\dot{q}_c$ , and the wheel rotational velocities  $\omega_W = [\omega_{1y}, \omega_{2y}, \omega_{3y}]^T \in \mathbb{R}^3$  using the above conditions. Using the Moore-Penrose pseudoinverse of  $A$  to solve for  $\dot{q}_c$  in (13), it follows that,

$$\dot{q}_c = (A^T A)^{-1} A^T B \dot{q}. \quad (14)$$

$$\Rightarrow \dot{q}_c = J \dot{q}. \quad (15)$$

Imposing a no-slip condition, the following must be true,

$$(A(A^T A)^{-1} A^T - I_{9 \times 9}) B \dot{q} = 0. \quad (16)$$

When (11) for each wheel is found and substituted into (16),  $\dot{q}$  cannot be solved for since  $(A(A^T A)^{-1} A^T - I_{9 \times 9}) B \dot{q}$  is not full rank. The uncontrolled variables  $\omega_{ir}$  and  $\omega_{iz}$  can be written in terms of wheel angular velocity,  $\omega_{iy}$ . Through algebraic manipulations, the transformation from wheel rotational velocities to body velocities is found to be,

$$\begin{bmatrix} u_c \\ v_c \\ \omega_{zc} \end{bmatrix} = \begin{bmatrix} -\frac{2R}{3} & \frac{R}{3} & \frac{R}{3} \\ 0 & -\frac{R}{\sqrt{3}} & \frac{R}{\sqrt{3}} \\ -\frac{R}{3L} & -\frac{R}{3L} & -\frac{R}{3L} \end{bmatrix} \begin{bmatrix} \omega_{1y} \\ \omega_{2y} \\ \omega_{3y} \end{bmatrix}. \quad (17)$$

It should be noted that the velocity of the vehicle is no longer dependent on the roller rotational velocity,  $\omega_{ir}$ . Inverting (17) allows to solve for the individual wheels speeds given a commanded body velocity vector  $\dot{q}_c = [u_c, v_c, \omega_{cz}]^T$ . Thus, from (6), the simulated plant dynamics outputs are converted to wheel velocities for the kinematic simulator platform,

$$\begin{bmatrix} m & 0 & 0 \\ 0 & m & 0 \\ 0 & 0 & I_{zz} \end{bmatrix} \begin{bmatrix} \dot{u} \\ \dot{v} \\ \dot{\omega}_z \end{bmatrix} = \begin{bmatrix} 0 & 0 & -mv \\ 0 & 0 & mu \\ mv & -mu & 0 \end{bmatrix} \begin{bmatrix} u \\ v \\ r \end{bmatrix} + \begin{bmatrix} f_x \\ f_y \\ \tau_z \end{bmatrix} \quad (18)$$

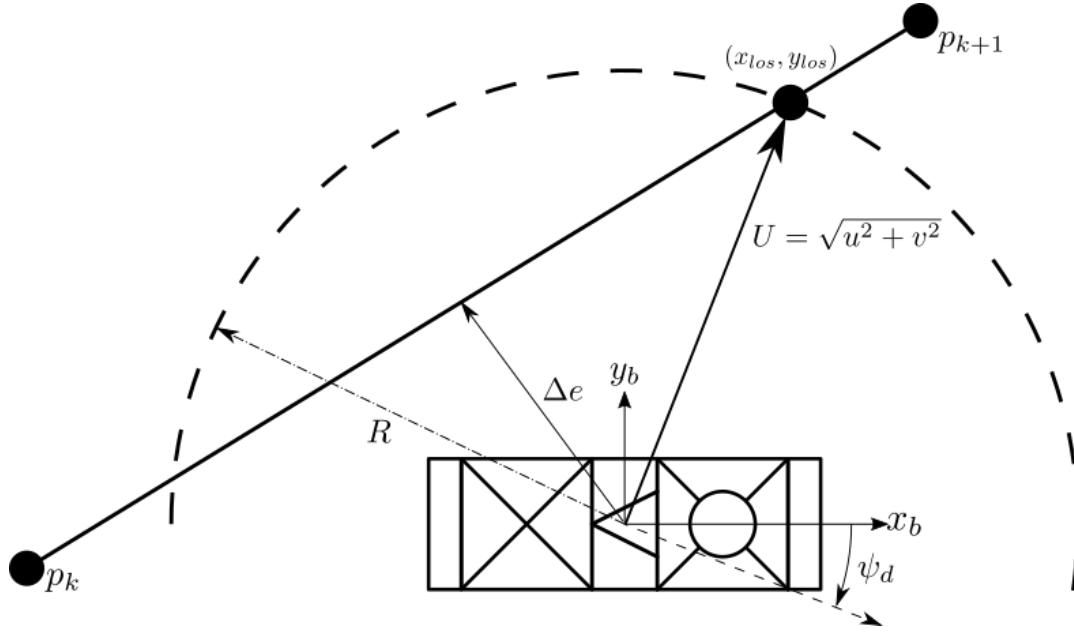


**Figure 6 – The “Enclosure Based Steering” guidance law. The main benefit of this guidance law is that it allows an underactuated system, like the 3U CubeSat, to minimize the cross track error  $\Delta e$  on a path between two waypoints,  $p_k$  and  $p_{k+1}$ . The steering law produces a desired orientation that guides the system to an intermediate waypoint  $(x_{los}, y_{los})$  at the intersection of a circle around the system and the path.**

$$\begin{bmatrix} \omega_{1y} \\ \omega_{2y} \\ \omega_{3y} \end{bmatrix} = \begin{bmatrix} -\frac{1}{R} & 0 & -\frac{L}{R} \\ \frac{1}{2R} & -\frac{\sqrt{3}}{2R} & -\frac{L}{R} \\ \frac{1}{2R} & \frac{\sqrt{3}}{2R} & -\frac{L}{R} \end{bmatrix} \begin{bmatrix} u \\ v \\ \omega_z \end{bmatrix}. \quad (19)$$

### Mission Planning and Controls

The guidance and control laws are given in this section – however, the navigation and attitude determination filters are excluded out of brevity. In brief, the navigation and attitude determination filters are extended Kalman filters based off of the approach in Crassidis and Junkin<sup>5</sup>, where a known inertial attitude or position solution from the SVGS is filtered with body rates and accelerations from the IMU. This allows the position and attitude estimates to continue to be propagated when no SVGS solution is present (i.e., target is out field of view or the SVGS is in between solutions).

### Guidance and Steering

The 3U CubeSat has a thruster configuration with thrust forces exclusively on the +Y and –Y faces of the spacecraft. Thus, the thrusters can only provide a force in the  $y_b$  axis, and a torque about the  $z_b$  axis. The underactuation of this system lends itself well to guidance and steering laws for marine vehicles, as most marine vessels are underactuated. An “Enclosure Based Steering” approach from Fossen<sup>6</sup> is taken to minimize

the cross-track error  $\Delta e$  and guide the spacecraft along a desired path between waypoints. Note that this is a path following approach rather than true trajectory tracking as there is no time dependence on the desired state  $\{x_d, y_d, \psi_d\}$  of the system.

Figure 6 depicts the main components of the Enclosure Based Steering law. The path between two desired waypoints  $p_k \in \mathbb{R}^2$  and  $p_{k+1} \in \mathbb{R}^2$  can be taken to be a straight line. A circle of radius  $R \in \mathbb{R}^+$  is circumscribed around the vehicle. For a sufficiently large  $R$ , the circle will intersect the path at two distinct points. The point in the direction of travel,  $(x_{los}, y_{los}) \in \mathbb{R}^2$  is taken to be an intermediate waypoint that a line-of-sight (LOS) steering law guides the vehicle towards. The desired orientation of the system from the LOS guidance is calculated as,

$$\psi_d = -atan2 \left[ \frac{x_{los}-x}{y_{los}-y} \right]. \quad (20)$$

Thus, the cross track error  $\Delta e \in \mathbb{R}$  is minimized by bringing the system back to the path that is “snapped” between waypoints. The calculation to obtain  $(x_{los}, y_{los})$  is left from this work, but can be found in full in Fossen<sup>6</sup>.

### Control Systems

The 3U satellite has two main control effectors – a reaction wheel assembly (RWA) for fine attitude control and a reaction control system (RCS) to provide “coarse”

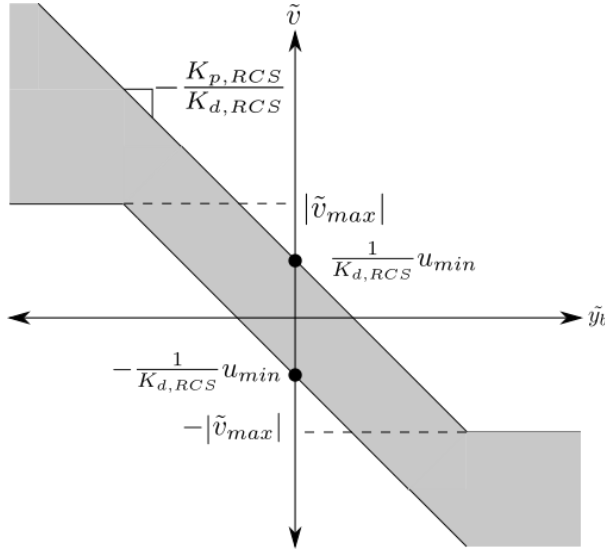


**Figure 7 – The RCS phase plane controller design. Areas highlighted in gray depict the deadband of the controller. All other areas would prompt either a positive (above switching lines) or negative (below switching lines) thruster firing.**

attitude corrections and translations. A proportional-integral-derivative (PID) controller drives the RWA control system, while a phase plane controller is responsible for RCS control. A mode controller dictates the criteria that causes the switch between the control systems.

The RWA controller provides a small amount of torque to the body through a change in the angular momentum of the wheels. A torque command is generated from a common PID controller,

$$\tau_{RWA} = K_{p,RWA}\tilde{\psi} + K_{i,RWA} \int \tilde{\psi} dt + K_{d,RWA}\dot{\tilde{\psi}}. \quad (21)$$

where  $\tilde{\psi} \in \mathbb{S}$  is the error in angular orientation of the vehicle from the desired value,  $\tilde{\psi} = \psi_d - \psi$ , and  $K_{p,RCS}$ ,  $K_{i,RCS}$ , and  $K_{d,RCS}$  are the PID gains, respectively.

The CubeSat is equipped with a 1,1,1-3,3,3-hexafluoropropane-based, green propellant reaction control system. The RCS is tasked with primarily translating the spacecraft between desired waypoints, but has the capability to induce a torque about the  $z_b$ -axis. This can be used in active steering or simulating a “detumble” scenario. For brevity, only the translation controller is described here.

The translation controller for the RCS system uses a phase plane design to guide the spacecraft towards a desired waypoint. Most autonomous rendezvous and

docking platforms use a fully actuated thruster configuration – both its lateral and longitudinal velocities can be controlled. The 3U design is underactuated and relies on the Enclosure Based Steering approach to guide the vehicle towards an intermediate waypoint to minimize cross tracking error. A single longitudinal controller operates on the  $y_b$  axis of the vehicle.

The phase plane controller can be expressed as a discontinuous function of the error in position in the body frame,  $\tilde{y}_b \in \mathbb{R}$ , and the velocity,  $\tilde{v} \in \mathbb{R}$ ,

$$u_{RCS} = K_{p,RCS}\tilde{y}_b + K_{d,RCS}\tilde{v}. \quad (22)$$

$$f_{RCS} = \begin{cases} -f_{RCS}, & u_{RCS} < -u_{min} \text{ and } \tilde{v} < |\tilde{v}_{max}| \\ f_{RCS}, & u_{RCS} > u_{min} \text{ and } \tilde{v} > -|\tilde{v}_{max}| \\ 0, & \text{otherwise} \end{cases} \quad (23)$$

where  $K_{p,RCS}$  and  $K_{d,RCS}$  dictate the slope of the switching line,  $\pm u_{min} \in \mathbb{R}$  determines the y-axis intercepts, and  $\tilde{v}_{max}$  limits the maximum velocity of the spacecraft. Figure 7 depicts the phase plane controller switching lines, with the grayed-out area in-between them denoting the deadband of the controller – the combination of  $\tilde{y}_b$  and  $\tilde{v}$  that produce no thruster firings. It can be readily seen that a system with initial conditions at an arbitrary point in the phase plane will be driven towards a neighborhood around the origin.

## SMARTPHONE VIDERO GUIDANCE SENSOR

The SVGS is a Marshall Space Flight Center-developed sensor that obtains the relative position and orientation between a camera and a known target. An interchangeable set of retroreflective targets or LEDs are used to create a pattern denoting the target. The camera images the target, lightly process the image to obtain the target blobs, and performs photogrammetric operations to obtain a relative distance and orientation from the camera frame to the target frame. A predecessor, the Advanced Video Guidance Sensor (AVGS), was flown on the DART and Orbital Express missions in 2005 and 2007, respectively. SVGS is the evolution of AVGS technology, reducing the form factor to that of a “smartphone.”

To calculate the 6DOF states between the camera and the target, the SVGS uses an inverse perspective algorithm with an adaptation of the collinearity equations<sup>7, 8</sup>. Given a thin lens camera, an object  $A$  has all its light rays entering the camera at a point  $L$ , known as the perspective center. An image of  $A$  will be formed on the camera plane, annotated by  $a$ . Figure 8 displays these objects, along with two frames – the object (target)

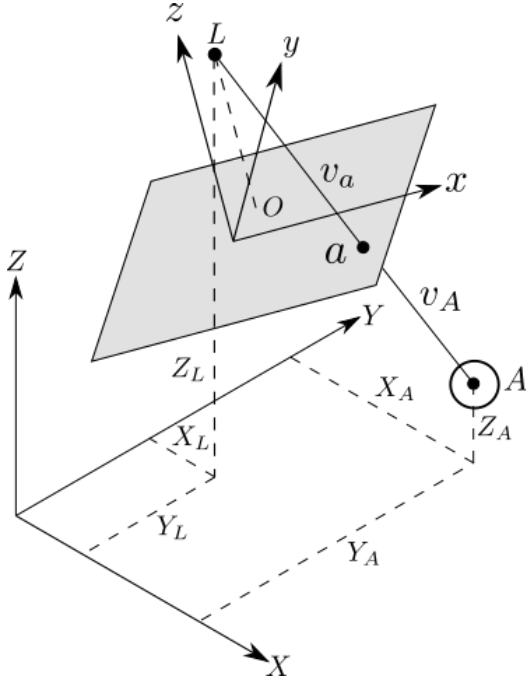


**Figure 8- Object (A) and camera frame (gray) geometry.**

coordinate system,  $\{X, Y, Z\}$ , and the image (chaser) coordinate system,  $\{x, y, z\}^1$ .

A vector from the perspective center to point  $A$  is defined as,

$$v_A = \begin{bmatrix} X_A - X_L \\ Y_A - Y_L \\ Z_A - Z_L \end{bmatrix}. \quad (24)$$

Another vector is defined from the perspective center to  $a$ ,

$$v_a = \begin{bmatrix} x_a - x_0 \\ y_a - y_0 \\ -f_o \end{bmatrix}, \quad (25)$$

where  $f_o$  is the vertical distance to point  $L$ . This new vector is simply a rotation and scaling of  $v_A$  as,

$$v_a = kT_A^a v_A. \quad (26)$$

Dropping the  $a$  and  $A$  subscripts, solving for the image frame coordinates  $x$ ,  $y$ , and  $z$ , and eliminating the scaling factor  $k$  by dividing by  $z$  yields,

$$x = f_o \frac{T_{11}(X - X_L) + T_{12}(Y - Y_L) + T_{13}(Z - Z_L)}{T_{31}(X - X_L) + T_{32}(Y - Y_L) + T_{33}(Z - Z_L)} + x_0 = F_x \quad (27)$$

$$y = f_o \frac{T_{21}(X - X_L) + T_{22}(Y - Y_L) + T_{23}(Z - Z_L)}{T_{31}(X - X_L) + T_{32}(Y - Y_L) + T_{33}(Z - Z_L)} + y_0 = F_y \quad (28)$$

where  $T_{ij}$  are the elements of the transformation matrix. The relative 6DOF state vector is given by,

$$V = [X_L, Y_L, Z_L, \phi, \theta, \psi]^T. \quad (29)$$

Performing a Taylor series expansion on (27) and (28), and then linearizing produces,

$$x = F_x(V_0) + \frac{\partial F_x}{\partial V} \Delta V + \epsilon_x, \quad (30)$$

$$y = F_y(V_0) + \frac{\partial F_y}{\partial V} \Delta V + \epsilon_y, \quad (31)$$

where  $V_0$  is an initial guess for the state vector, and  $\Delta V$  is the difference between  $V_0$  and the actual state vector,

$$\Delta V = V - V_0. \quad (32)$$

$\epsilon_x$  and  $\epsilon_y$  are the error terms associated with the linearization of (27) and (28). The SVGS target contains four feature cubes, each of which is a known distance from the target origin. Each will have two set of equations corresponding to  $F_x$  and  $F_y$  as above,

$$Y = [x_1, y_1, \dots, x_4, y_4]^T \quad (33)$$

$$Y_0 = [F_{x1}, F_{y1}, \dots, F_{x4}, F_{y4}]^T$$

$$H = \left[ \frac{\partial F_{x1}}{\partial V}, \frac{\partial F_{y1}}{\partial V}, \dots, \frac{\partial F_{x4}}{\partial V}, \frac{\partial F_{y4}}{\partial V} \right]^T$$

Thus, the vectorial representation of (30) is written as,

$$Y = Y_0 + HV + \epsilon. \quad (34)$$

The equation above is solved for the  $V$  that most minimizes the square of the residuals  $\epsilon$ . This value is then added to  $V_0$  to get an updated state vector. This process is iterated until the residual are sufficiently small yielding the final estimate of the 6DOF state vector  $V$ .

The process described above is implemented on an Android smartphone. Accuracy and solution rate are highly dependent on the processor of the platform, as well as the resolution of the image. Accuracy and a faster

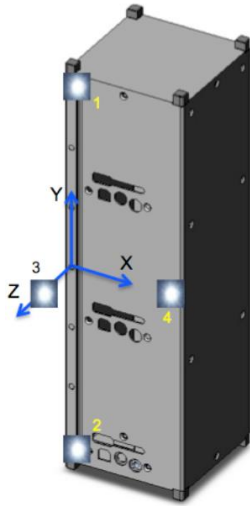


**Figure 9 – SVGS target pattern configuration using retroreflective cubes, with the center cube out of plane. The target frame is denoted in blue.**

update rate can be traded off by decreasing the image size (less accurate, faster update) or increasing it (more accurate, slower update). The experiments described in this text utilize a legacy platform, the Samsung Galaxy Nexus, with a 1.2GHz dual core ARM Cortex-A9 processor. With a maximum supported image size of 1920 x 1080 pixels, an update rate of 4Hz can be achieved. The SVGS algorithm has been ported to a newer model, the Samsung S8, with a 2.35/1.9 GHz octa-core Qualcomm Snapdragon processor. A solution rate of up to 33Hz has been achieved on this platform at the same 1920 x 1080 pixel image size.

The target configuration is wholly left to the user. Solutions have been more successful when at least a single target cube is out of plane with respect to the others. The target configuration utilized in the experiments described here is composed of four retroreflective cubes as shown in Figure 9. The retroreflective cubes were placed such that they would fit within a 3U footprint.

## PLATFORM INTEGRATION AND AVIONICS

The 3U CubeSat is outfitted with a conventional sensor and avionics suite, as well as an SVGS. An ADIS16488 IMU is the main inertial sensor for the platform. A Sinclair Sun Sensor is utilized to obtain a partial attitude solution and to test “safe mode” behaviors. A custom developed board running a 32-bit TIVA processor is used to preprocess the sensor output, and optionally, run attitude and navigation filters. These sensors are located on the navigation stack of the 3U and can be optionally placed on the ASKS platform.

A MAI reaction wheel assembly is used for fine pointing control. It features full three-axis control with  $\sim 11\text{mN}\cdot\text{m}\cdot\text{s}$  of capacity and a maximum torque of  $0.635\text{mN}\cdot\text{m}$ . This RWA can be swapped with a single axis  $30\text{mN}\cdot\text{m}\cdot\text{s}$  reaction wheel from Sinclair capable of producing  $2\text{mN}\cdot\text{m}$  of torque. A custom developed cold-gas propulsion unit from the University of Arkansas is used for translational control as well as coarse attitude corrections and detumble. It utilizes a green propellant, 1,1,1-3,3,3-hexafluoropropane, with a nominal ISP of 47s. Although the effectors cannot be utilized on the ASKS platform, high fidelity models of each have been developed and are simulated within the ASKS plant dynamics. This lends itself to situations where each effector is “plug-and-play.” For instance, if the ASKS system is exhibiting sluggish response utilizing the  $0.635\text{mN}\cdot\text{m}$  MAI reaction wheel, this component can be “swapped” for the higher capacity Sinclair  $2\text{mN}\cdot\text{m}$  reaction wheel.

The Xiphos Q7 was selected as the flight computer, due to its easy integration with the core software package of ROS and the ability to run a near-real time Linux OS. The latter is especially important when working with students and interns. It has been the authors’ experience that the prevalence of cheap single board computers (e.g., Raspberry Pi, Beaglebone Black, Pixhawk, etc.) in the hobbyist markets and educational facilities has exposed many students to embedded systems running a lightweight OS. Often, students come into an internship with an already-developed skillset in building software for embedded Linux devices. This expertise that can be leveraged and directed towards aerospace system during their term.

## SOFTWARE ARCHITECTURE

### *Software Architecture*

Software development is scheduled in two major phases, as shown in Figure 10. In Phase I, the onboard gyroscope and accelerometer of the Galaxy Nexus is used for feedback, and the GNC algorithms are run from within the phone, alongside the plant dynamics. This is all programmed within a Java/Android environment. The EV3 “brick,” the microcontroller regulating the motors and communicating with the Galaxy Nexus, runs the “LeJOS” operating system – an alternative, Java-based OS developed by the LEGO community. During Phase I development, the only necessary piece of hardware is the SVGS compatible phone – all sensors and simulation suites are hosted on it.

For Phase II development, the navigation stack is integrated onto Agilis platform as modeled in Figure 2. This allows for the “flight” IMU, the ADIS16488, to be used for feedback in the control system, as well as



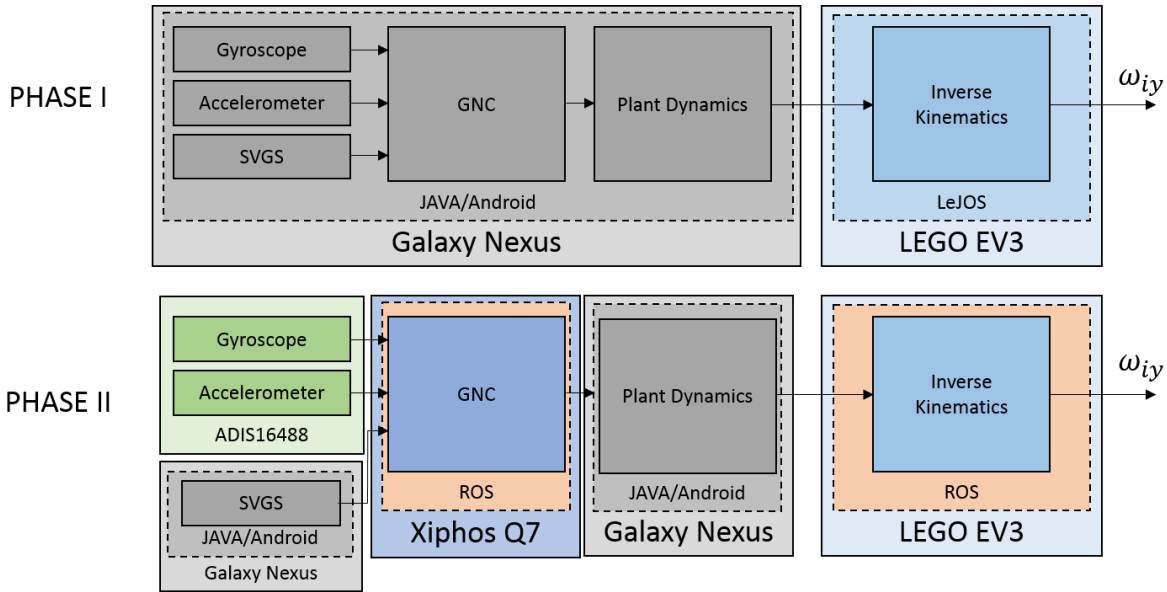


**Figure 10 – Phase I and Phase II software block diagrams for the Agilis kinematics simulator platform. For Phase I, all GNC and plant dynamics are run directly on the android phone, using the onboard gyroscope and accelerometer. Phase II uses the “flight” IMU, the ADIS16488 as the main inertial sensor, and moves the GNC software to the Xiphos Q7 to enable processor-in-the-loop simulations**

enabling processor-in-the-loop simulations. The Robot Operating System is chosen as the main environment to tie these systems together. Both the Xiphos Q7 and the LEGO EV3 are both capable of running the core ROS package. The publish/subscribe model of ROS interprocess communication eases the development of the interfaces between these systems, as well as gives access to full featured front-end GUIs. The end goal of the second phase of development is to have a full flight-like navigation stack running on the ASKS, creating a partial physical realization of the plant with hardware-in-the-loop capabilities.

A key benefit of the ASKS architecture is in its capability for the rapid redevelopment and deployment of the GNC system. This is enabled through the use of the Simulink Coder, Embedded Coder, and a wrapper using the Java Native Interface (JNI). This wrapper is used exclusively for Phase I development. For Phase II development, the GNC source code can be integrated directly into a ROS project, and compiled into a separate ROS node. This permits a greater level of modularity when swapping in and out different GNC systems when compared with Phase I development.

The GNC system, as well as the plant model, for the 3U CubeSat is modeled in Mathworks Simulink – a visual-based tool for time domain simulation, with the capacity to analyze a system in the frequency and  $s$ -domains. The creation of GNC flight software can be streamlined by taking advantage of Simulink Coder and Embedded

Coder – “toolboxes” that compile a Simulink block diagram into C or C++ source code. Embedded Coder allows for greater control of the “autogenerated” source code with the ability to target specific platforms, such as ARM-based or Microchip (PIC) architectures. JNI is a framework that allows native programs to be called from the Java Virtual Machine (JVM). The recommended platform for Android app development, the IntelliJ-derived Android Studio, allows for the easy integration of native source code (e.g., C or C++) into Android projects through the CMake build system.

The workflow for testing on the ASKS platform functions as follows: the GNC system and plant model are initially developed within Simulink with Matlab helper scripts to setup parameters. Gains and filter coefficients are optimized within that environment to produce the “best” response given mission requirements. Then, the GNC system and the plant model are separately configured and autotyped. This produces two software packages – one for GNC and one for the plant. For Phase I development, both of these codebases are integrated directly within an Android app through a wrapper using the JNI. This same app runs the SVGS process in the background, producing relative orientation and position estimates that are fed into the GNC system as pictured in Figure 10. The app queries telemetry from the onboard gyroscope and accelerometer, which are also used as inputs to the GNC system. The GNC system is run for a single time step, and its outputs (actuator commands) are piped to the plant dynamics. The body

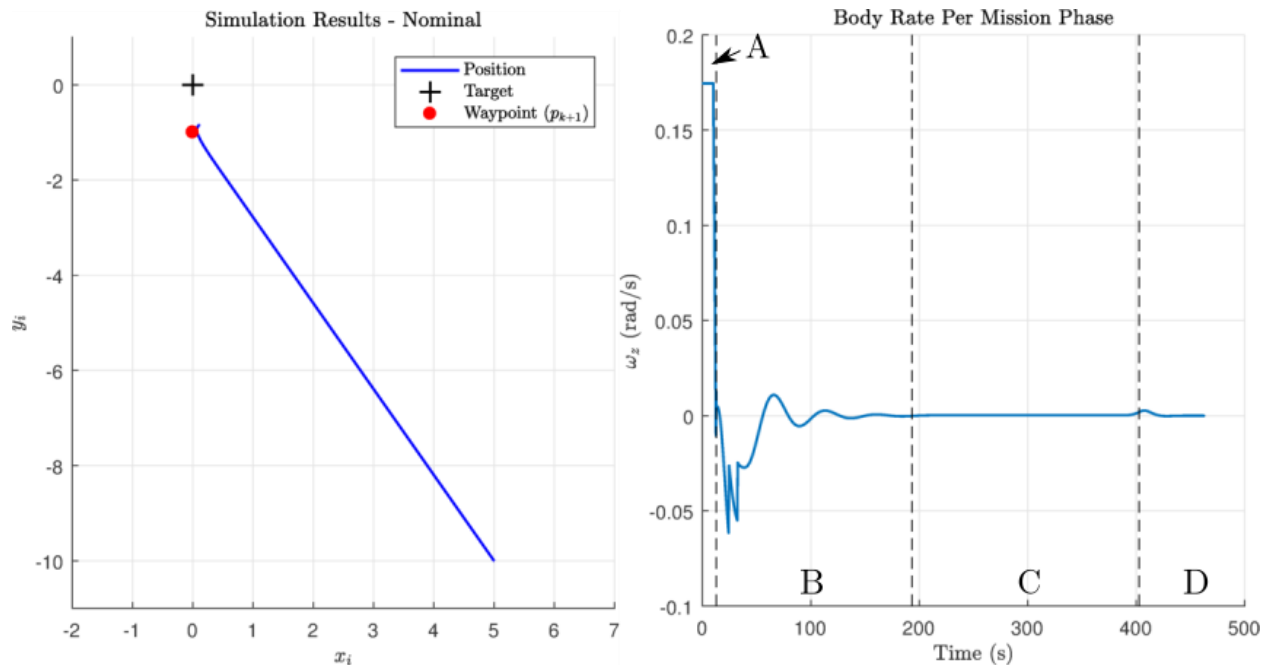


**Figure 11 – Simulation results for the rendezvous operation described above. The spacecraft’s position is shown on the left in blue, with the desired waypoint  $p_{k+1}$  in red. The target position is specified in black. On the right, the spacecraft body rate  $\omega_z$  is broken down by mission phase: A) detumble and target search, B) slew towards target, C) translation towards desired waypoint, D) reorientation to guide towards waypoint.**

velocities  $u$  and  $v$  and rotation rate  $\omega_z$  are then converted to ASKS wheel velocities  $\omega_{iy}$ . These are then sent as motor commands to the EV3 “brick” motor controller. The simulated 3DOF platform can now be run and its response logged. Depending on the performance during the experiment, the GNC system can be easily updated simply by tweaking parameters, or if a structural change is needed (e.g., increasing the order of a filter, adding a gain in path where one was not included, etc.), the GNC system can be autocoded and deployed to the Android app. The latter typically takes less than five minutes to go from a Simulink block diagram to an application running on the ASK.

### Robot Operating System

The Robot Operating System (ROS) provides a flexible framework to create an autonomous system/robotic middle layer on top of an operating system<sup>9</sup>. It handles message passing (on a centralized publisher/subscriber model) and comes bundled with package control. Many features are available “out-of-the-box” through ROS packages, such as Kalman filter implementations and visualization software. ROS is compatible with a variety of popular platforms including the Microsoft Kinect, a three dimensional camera originally designed for the Microsoft Xbox 360, and the Beaglebone Black, a single-board computer that is popular in the hobbyist community. ROS has been applied to differing platforms

in radically different environments, including personal robotics<sup>9</sup>, marine vehicles<sup>10</sup>, intravehicular robotics on the International Space Station<sup>11</sup>.

One important distinction is that ROS is not a real-time operating system (RTOS), nor is it out-of-the-box compatible with other RTOS, such as FreeRTOS and VxWorks. However, ROS does excel at ease of use, with a large online community and easily available tutorials. It has been the experience of the authors that real-time programming has a relatively steep learning curve for students unfamiliar with RTOS concepts (e.g., tasking, priority levels, semaphores, etc.). Transitioning the software architecture from RTOS to ROS-based significantly decreased the learning curve from 4-6 weeks to 1-2 weeks. Additionally, the availability of ROS sample code further streamlined development in later stages, as students could modify existing code rather than reproduce it wholesale.

Language implementation is equally as important. ROS is available both in C++ and Python. RTOS are typically only available in C and C++, since both of these languages compile down to native machine code rather than rely on a non-deterministic virtual machine. It has been the authors’ experience that engineering students across all levels have a greater familiarization with the Python language when compared to C, and especially C++.

## SIMULATION AND EXPERIMENTAL RESULTS

### Simulation Results

Simulations of the autonomous rendezvous procedure were produced using the Matlab/Simulink software suite from Mathworks. The SVGS target frame was taken to be coincident with the inertial frame, i.e., the spacecraft started the simulation at an arbitrary point in the mission area and then was guided towards the origin to perform a proximity operation.

The simulation tasked the vehicle to perform four separate tasks in order:

1. Detumble from an initial tip-off rate.
2. Perform a target search.
3. Slew towards the target.
4. Translate to a meter in front of the target.

The results presented here set an initial tip off rate at 10deg/s, and positioned the spacecraft 5m and -10m from the target in the X and Y axis, respectively. The mission area of this simulation roughly fits the footprint of the portion of the flat-floor facility at Marshall Space Flight Center that is dedicated for small satellite testing. A desired “waypoint” was set -1m from the target in the Y axis.

Results show the spacecraft successfully detumbling utilizing the RCS thrusters, and proceeding towards a target search, finally homing in on the target at roughly ~25deg. For the latter maneuver, the mode controller switched the system to reaction wheel control. The spacecraft then translated toward the desired waypoint utilizing the Enclosure Based Steering guidance law. Once the SVGS was able to produce an attitude solution, a path was created between the current position ( $p_k$ ) to the desired waypoint ( $p_{k+1}$ ). The spacecraft then translated to approximately one meter in front of the target before the simulation completed successfully.

A strength of Enclosure Based Steering is its ability to compensate for outside disturbances. Simulation results from the Simulink model are displayed for a spacecraft with a faulted thruster, where an RCS thruster was misaligned by 10 degrees from the nominal orientation. A comparison between the cross track error during translation for an Enclosure Based Steering guidance law versus a simple LOS law,

$$\psi_d = -atan2 \left[ \frac{x_{k+1}-x}{y_{k+1}-y} \right], \quad (35)$$

is presented in Figure 12. It can be readily seen that the Enclosure Based Steering approach was able to bring the vehicle back to the desired path, whereas the pure LOS

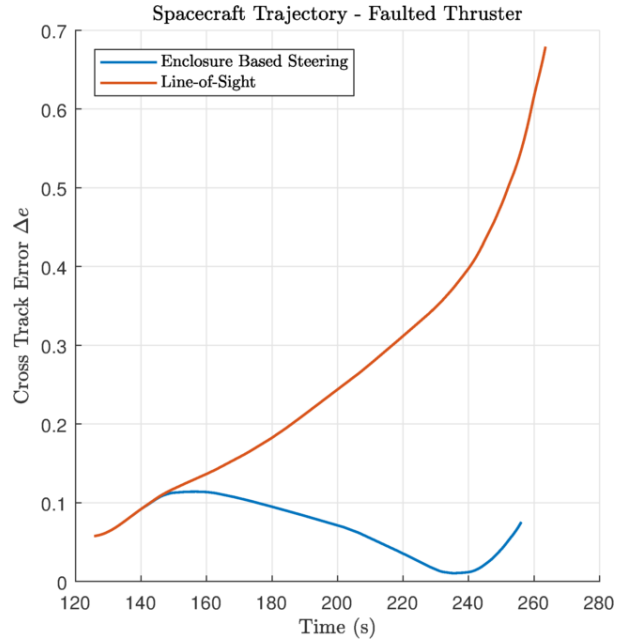


**Figure 12 – Comparison of cross track errors  $\Delta e$  between the Enclosure Based Steering and LOS guidance steering laws.**

guidance failed to do so, incurring a cross track of up to 0.7m.

### Experimental Results

Experimental results are presented for a subset of the tasks described in the previous section. The experiment focused exclusively on “detumbling” the satellite, then slewing towards the target, and performing an attitude hold for a set duration of time (tasks 1-3 as described previously). This is analogous to a spacecraft detumbling after ejection, followed by moving into a stable pointing orientation (e.g., a solar inertial hold, or relative hold on a target). The ASKS was outfitted with the “Phase I” avionics architecture depicted in Figure 10 to perform these experiments.

The ASKS platform was placed approximately one meter away from the target at a slight offset of 2cm. For this series of tests, the accelerometer was disabled, and the position output was directly taken from the SVGS. If the SVGS failed to find a solution, the last valid solution was latched. The attitude filter was similarly modified where the SVGS attitude solution was taken to be the attitude estimate of the system without fusing gyroscope measurements. If the SVGS was not able to produce an attitude solution, the filter would then propagate the attitude estimate using the body rate measurements.

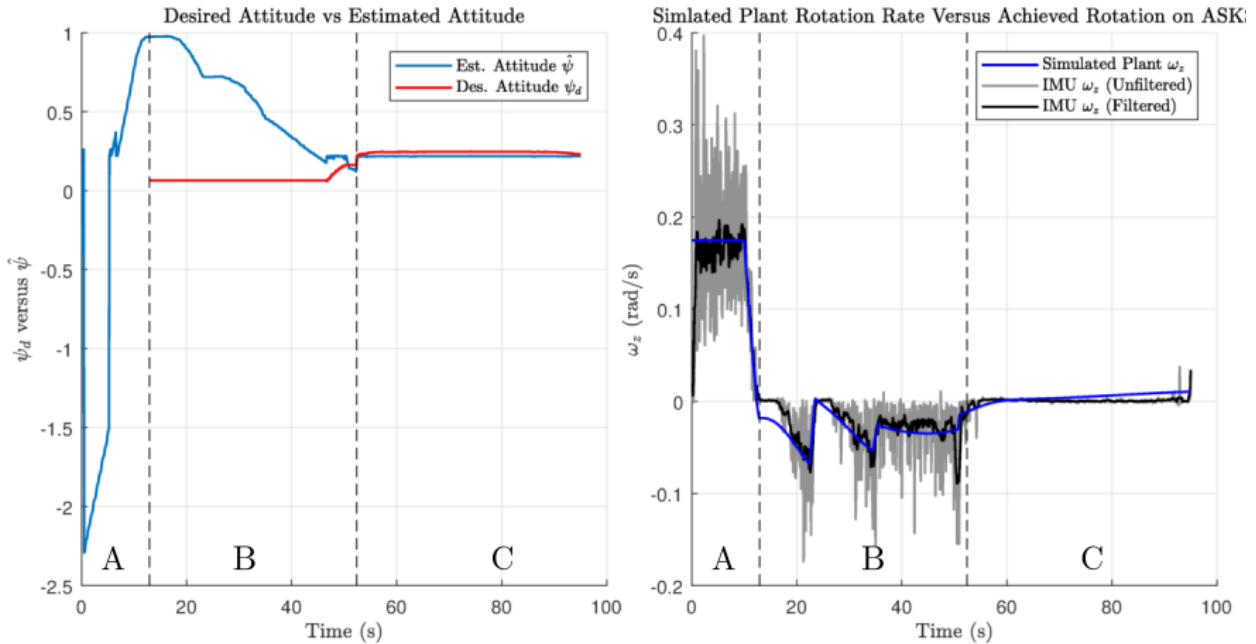


**Figure 13 – Results from the experimental test with the ASKS performing a detumble (A), slew (B), and hold and point (C) maneuvers. The desired attitude  $\psi_d$  (blue) is compared against the estimated attitude  $\hat{\psi}$  (red) from the attitude filter on the left. The right displays the simulated plant rotation rate (blue), the unfiltered IMU rate from the ASKS platform (gray) and the filtered rate signal (black).**

Figure 13 presents the results from experimental test. The figure on the left displays the commanded attitude  $\psi_d$  in blue and the estimated attitude  $\hat{\psi}$  in red. On the right, there is a comparison between the simulated plant rate  $\omega_z$ , the unfiltered ASKS platform IMU rate (gray), and the filtered IMU rate (black). The three main phases are demarked in each figure by the vertical dashed line: the detumble phase (A), the slewing maneuver (B), and the “hold and point” maneuver (C). The system utilizes a bang-bang controller with the RCS for the detumble phase, and a fine pointing reaction wheel control for the remainder of the phases. Examining both figures, it is clear that the kinematic simulator platform detumbled successfully, with the rotation rate of the platform dropping to zero for both the simulated plant and ASKS IMU. It is noteworthy that the filtered IMU signal closely matched that of the simulated plant output, signifying that the inverse kinematic operation from the spacecraft body velocities and rate to Agilis wheel velocities was successful. The remainder of the experiment continued to be successful in this regard, with the sensed rate of the ASKS platform closely trending with the simulated plant output. In the second phase, the system was tasked to perform a slew towards the target. A desired orientation  $\psi_d$  was constructed from the estimated position of the ASKS to the *a priori* target position such that the SVGS would acquire a successful solution. A position solution was first obtained during the detumble operation, where the target passed in the line of sight of the SVGS. This

solution was then maintained during the slewing maneuver, which did not have the successful lock on the target until the 45s mark. A noticeable drift then occurred in the desired attitude signal as the SVGS reacquired a lock on the target and produced an updated attitude and position solution. The remainder of the mission demonstrates a successful attitude hold maneuver with the SVGS maintaining the target in its sights. The reader may note a small offset between the desired orientation and the estimated orientation. This is the result of two main causes. The first is due to a quantization effect when requesting a wheel velocity from the LEGO EV3 controller. During phase C), the steady state error was not large enough to overcome this quantization given the gains on the RWA PD controller. For this particular run, the integral gain  $K_i$  was disabled for the RWA controller, which did not allow the steady state error to accumulate over time. This would have built up a control signal large enough to dominate the quantization. As part of a redesign of the ASKS platform, the gearing ratio will be stepped down such that a larger motor command will produce a lower wheel speed, allowing for finer control of the platform.

## EDUCATIONAL OUTREACH

A variety of students with varying skill sets have contributed to this project. These have spanned the academic spectrum from high school seniors to graduate students. The authors serve only as system integrators

and mentors – the majority of the development of this project has been contributed by students, interns, and volunteers. The following section relays the experience of the authors’ in working with these students. It is not intended to be an impartial assessment, but rather, is a series of best practices that the authors’ have found to be successful.

The multidisciplinary aspects of the ASKS platform are used to its advantage. A range of disciplines are used to create the platform, which allows mentors to select the strengths of each student and direct them to develop along that particular path. These disciplines are broken down across the columns of Table 1 – mechanical design, avionics and software, GNC, and SVGS development. The rows give the educational level of each student and tasks that he or she is likely best suited for.

Through educational outreach programs in public schools, high school students have worked on ASKS development. These students are high performing, but have only had a fraction of the courses taught in a college engineering program. However, traditional high school engineering curriculums stress computer aided design (CAD). With the advent of low-cost 3D printers, students now have the complete experience of designing a part and manufacturing a prototype. This experience is leveraged in this project where students are given requirements for a single part, and must deliver a prototype by the end of their rotation. This gives a “hands on” introduction to the engineering development cycle. These students often have some experience in calculus and basic linear algebra, but typically have not had an opportunity to use it in practice. The ASKS platform serves as a test bed for this purpose. Concepts such as integration and derivation (through the vehicle acceleration, velocity, and position), matrix inversion (through the inverse kinematic relation in (18) and (19)) and gear ratios are given a physical anchor. The selection of Java as one of the main languages for this project leverages its continued use in Advanced Placement computer science courses, as well as its popularity in Introduction to Computer Science and object-oriented programming courses. Although high school students may not have the skillset to make significant development in the codebase, they can make small modifications to deploy different concepts. The use of LEGO robots and cellular phones creates an approachable environment where students are familiar with the toolset, creating a launch point for furthering their knowledge of small satellites and general engineering.

Students further along in academic level, like later college or early graduate school, get introduced to

concepts that are more specified. These include image processing, computer vision, Kalman filters, and control systems. The latter two are especially important as many engineering curriculums do not focus heavily on GNC, and may not sufficiently bridge the gap between theory and practice. Students may have some familiarization with concepts like PID controllers and linear filters, but have not had the opportunity to exercise them in a design environment. The ASKS provides this opportunity with its ability to rapidly redeploy the entire GNC system. Upper level students have contributed to this program in terms of software development both on the avionics platforms and the SVGS, as well as implementation of controllers and mission planners for wheeled vehicles.

Students of all levels have contributed to this project as described below:

- Design of mechanical interfaces and mounts between the navigation stack and the Agilis robot.
- Design of mechanical interfaces between the SVGS phone and target and the Agilis robot.
- Construction and implementation of PID controllers and mission planners for wheeled vehicles and CubeSats.
- Construction and implementation of navigation filters using an extended Kalman filter for position estimation on wheeled vehicles and CubeSats.
- Low-level device drivers for Linux systems wrapped in ROS nodes.
- Software architecture design in the ROS environment for the GNC system
- Processor-in-the-loop testing of the Xiphos Q7 with the GNC system in a ROS environment.
- Development of graphical user interfaces to log telemetry and display telemetry from the ASKS/CubeSat system.
- Extension of the SVGS blob tracking algorithm to work with colored LEDs in addition to retroreflective targets.
- Refactoring and documentation of SVGS software.
- Development of interfaces between LEGO EV3 “brick” and Android smartphone.

A diversity of “soft skills” have also been introduced as part of this project. These skills apply in breadth of fields and range from professional writing, mentoring, as well as configuration management. Concepts such as interface control documents are introduced such that each students work can be taken to be a “black box” that interfaces with the rest of the system.

**Table 1 – Recommended roles and responsibilities for a multidisciplinary project given a students’ level of education and experience.**

Academic Level	Mechanical Design	Avionics and Software	GNC	SVGS
High School	CAD’ing simple geometries, 3D printing parts, assembly and integration of systems	Introduction to Ohm’s law, power calculation, polarity. Java programming introduction.	Basic linear algebra introduction (e.g., determinants, matrix inversions).	Operation of SVGS.
Early College (Freshmen And Sophomores)	Advanced CAD’ing, coordination with high school interns for 3D printing.	Debugging of avionics interfaces, simple input/output programming.		Basic Java programming. Updating UI of SVGS.
Late College (Juniors And Seniors)	-	Integration of GNC project into ROS. Wrapping FC hardware drivers into ROS nodes. Processor-in-the-loop and hardware-in-the-loop simulations.	Designing of Kalman filters, redesign of control system gains, advanced mission planning (trajectory planning), integration of A* planner.	Enhancement of capabilities of SVGS outside of core engine (e.g., different blob tracking algorithms, optimizing implementation).
Graduate	-	-		

Internships at NASA range anywhere from 12 weeks in the Summer semester to 16 weeks in Fall and Spring Semesters. The key challenge is identifying a deliverable that each student is capable of producing within that time. There is no systematic process in assigning a student tasks – it has been the authors’ experience that one-on-one mentorship provides the best results for both parties. Mentors are better able to grasp the strengths of each student and assist them where necessary, and students are able to work on projects that align with their proficiencies.

## CONCLUSION

An alternative to “floating” CubeSat systems mounted on air bearings is given here, where the kinematics of the system can be represented by the motion of an omnidirectional wheeled vehicle equipped with rotacaster wheels. Plant dynamics are simulated within the wheeled robot to produce velocities and body rates. This allows the engineer to test high level guidance and navigation algorithms without the overhead of the traditional air-bearing method, which may be limited by mission area or length of air supply hoses. An omnidirectional robot is constructed out of LEGO EV3 parts and equipped with a smartphone-based relative navigation sensor, the SVGS, making it accessible as an educational platform. Multiple ASKS units may be constructed to simulate complex multi-satellite mission. The ASKS platform is detailed with a derivation of the inverse kinematic solution from 3DOF planar body velocities and rate to wheel speeds. Two separate control

laws are given – a phase plane controller focusing on the translational and coarse attitude control using a cold-gas RCS, and a PID controller for fine pointing control using reaction wheels. Due to the underactuation of the 3U CubeSat system the ASKS platform was based on, an Enclosure Based Steering approach is given to direct the vehicle back to a path between waypoints during translational control. Simulation and experimental results are presented of the 3U CubeSat and the ASKS platform operating in a proximity operation-like scenario. It was shown that the ASKS was able to successfully replicate detumble, slew, and attitude hold maneuvers of the 3U CubeSat.

## Forward Work

The system can be further improved in modeling the 3DOF planar motion of a satellite by increasing the gearing ratio between the motor and the wheels. For slow slews, as would be expected on a small satellite platform with small reaction wheels, a greater control of the position of each wheel of the Agilis is necessary. The authors’ noticed some limit cycle oscillations driven by quantization effects of the wheel controller on the EV3 robot. A smaller gearing ratio would allow a greater range of motion of each motor, reducing the impact of quantization.

The construction of multiple units allows for simulation of complex proximity operation missions and formation flying. This creates an easy to use platform for students, interns, and young engineers that enables the simulation

and testing of collaborative multi-satellite scenarios with familiar components.

### **Acknowledgements**

The authors would like to thank the following students for their contribution this work: Zachary Prihoda, Elijah Johnson, Amarri Cole, Tevon Walker, Eric Bradshaw, Dylan Hunziker, Chris Carter, Logan Bolingbroke, Zakk Giacometti, Brian Adams, James Holt, Bryce Brown, and Joshua Bryant. A special thanks to Devon Sanders for his support in the initial phases of this project.

### **REFERENCES**

1. C. Becker, R. Howard and J. Rakoczy, "Smartphone Video Guidance Sensor for Small Satellites," in *27th Annual AIAA/USU Conference on Small Satellites*, Logan, Utah, USA, 2013.
2. F. Terui, "Position and attitude control of a spacecraft by sliding mode," in *American Control Conference, Proceedings of*, Philadelphia, Pennsylvania, USA, 1998.
3. J. E. Prussing and B. A. Conway, *Orbital Mechanics*, New York City, New York, USA: Oxford University Press, 1993.
4. D. Garcia-Sillas, E. Gorrostieta-Hurtado, J. Vargas, J. Rodriguez-Resendiz and S. Tovar, "Kinematics modeling and simulation of an autonomous omnidirectional mobile robot," *Ingeniera e Investigacion*, vol. 35, no. 2, pp. 74-79, 2015.
5. J. L. Crassidis and J. L. Junkin, *Optimal estimation of dynamics systems*, CRC Press, 2011.
6. T. I. Fossen, *Handbook of marine craft hydrodynamics and motion control*, John Wiley & Sons, 2011.
7. F. H. Moffit and E. M. Mikhail, *Photogrammetry*, New York City, New York, USA: Harper & Row Inc., 1980.
8. J. Rakoczy, *Application of the photogrammetric collinearity equations to the orbital express advanced video guidance sensor six degrees-of-freedom solution*, MARshall Space Flight Center, AL: NASA Internal memo #XD-31-(-05-004), 2005.
9. M. Quigley, K. Conley, B. Gerkey, J. Faust, T. Foote, J. Leibs, R. Weeler and A. Y. Ng, "ROS: an open-source Robot Operating System," *ICRA workshop on open source software*, vol. 3, no. 3.2, p. 5, 2009.
10. J. Wampler, T. Mosciki and K. von Ellenrieder, "Towards adjustable autonomy for human-robot interaction in marine systems," in *OCEANS 2017 - Aberdeen*, Aberdeen, Scotland, UK, 2017.
11. J. Yoo, I.-W. Park, V. To, J. Q. Lum and T. Smith, "Avionics and Perching Systems of Free-Flying," in *AIAA SPACE 2015 Conference and Exposition, Systems Engineering (ISSE)*, 2015 IEEE International Symposium on, 2015.